



PAPER

Search for an interaction mediated by axion-like particles with ultracold neutrons at the PSI

OPEN ACCESS

RECEIVED

2 April 2023

REVISED

15 August 2023

ACCEPTED FOR PUBLICATION

27 September 2023




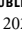
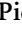
PUBLISHED

9 October 2023

Original Content from
this work may be used
under the terms of the
[Creative Commons
Attribution 4.0 licence](#).

Any further distribution
of this work must
maintain attribution to
the author(s) and the title
of the work, journal
citation and DOI.



N J Ayres¹, G Bison², K Bodek³ , V Bondar¹, T Bouillaud⁴, E Chanel^{5,13}, P-J Chiu^{1,2,14,*} , B Clement⁴, C B Crawford⁶, M Daum², C B Doorenbos^{1,2}, S Emmenegger¹, M Fertl⁷ , P Flaux⁸, W C Griffith⁹, P G Harris⁹, N Hild^{1,2}, M Kasprzak², K Kirch^{1,2}, V Kletzl^{1,2}, P A Koss¹⁰, J Krempel¹, B Lauss², T Lefort⁸, P Mohanmurthy^{1,2,15} , O Naviliat-Cuncic⁸, D Pais^{1,2}, F M Piegsa⁵, G Pignol⁴, M Rawlik¹, I Rienäcker^{1,2}, D Ries¹¹, S Rocchia⁴, D Rozpedzik³, P Schmidt-Wellenburg^{2,*} , N Severijns¹⁰, B Shen¹¹, K Svirina⁴, R Tavakoli Dinani¹⁰, J A Thorne⁵, S Touati⁴, A Weis¹², E Wursten^{10,16}, N Yazdandoost¹¹, J Zejma³, N Ziehl¹ and G Zsigmond²

¹ ETH Zürich, Institute for Particle Physics and Astrophysics, CH-8093 Zürich, Switzerland

² Paul Scherrer Institut, CH-5232 Villigen PSI, Switzerland

³ Marian Smoluchowski Institute of Physics, Jagiellonian University, 30-348 Cracow, Poland

⁴ Université Grenoble Alpes, CNRS, Grenoble INP, LPSC-IN2P3, 38026 Grenoble, France

⁵ Laboratory for High Energy Physics and Albert Einstein Center for Fundamental Physics, University of Bern, CH-3012 Bern, Switzerland

⁶ Department of Physics and Astronomy, University of Kentucky, Lexington, KY 40506, United States of America

⁷ Institute of Physics, Johannes Gutenberg University Mainz, 55128 Mainz, Germany

⁸ Normandie Université, ENSICAEN, UNICAEN, CNRS/IN2P3, LPC Caen, 14000 Caen, France

⁹ Department of Physics and Astronomy, University of Sussex, Falmer, Brighton BN1 9QH, United Kingdom

¹⁰ Instituut voor Kern- en Stralingsfysica, University of Leuven, B-3001 Leuven, Belgium

¹¹ Department of Chemistry—TRIGA site, Johannes Gutenberg University Mainz, 55128 Mainz, Germany

¹² Physics Department, Université de Fribourg, CH-1700 Fribourg, Switzerland

¹³ Present address: Institut Laue Langevin, 38000 Grenoble, France.

¹⁴ Present address: Physik-Institut, University of Zurich, CH-8057, Switzerland.

¹⁵ Present address: Massachusetts Institute of Technology, MA, United States of America.

¹⁶ Present address: RIKEN, Ulmer Fundamental Symmetries Laboratory, 2-1 Hirosawa, Wako, Saitama, 351-0198, Japan.

* Authors to whom any correspondence should be addressed.

E-mail: pin-jung.chiu@physik.uzh.ch and philipp.schmidt-wellenburg@psi.ch

Keywords: dark matter, axion, axion-like particle, beyond Standard Model physics

Abstract

We report on a search for a new, short-range, spin-dependent interaction using a modified version of the experimental apparatus used to measure the permanent neutron electric dipole moment at the Paul Scherrer Institute. This interaction, which could be mediated by axion-like particles, concerned the unpolarized nucleons (protons and neutrons) near the material surfaces of the apparatus and polarized ultracold neutrons stored in vacuum. The dominant systematic uncertainty resulting from magnetic-field gradients was controlled to an unprecedented level of approximately 4 pT cm^{-1} using an array of optically-pumped cesium vapor magnetometers and magnetic-field maps independently recorded using a dedicated measurement device. No signature of a theoretically predicted new interaction was found, and we set a new limit on the product of the scalar and the pseudoscalar couplings $g_s g_p \lambda^2 < 8.3 \times 10^{-28} \text{ m}^2$ (95% C.L.) in a range of $5 \text{ } \mu\text{m} < \lambda < 25 \text{ mm}$ for the monopole–dipole interaction. This new result confirms and improves our previous limit by a factor of 2.7 and provides the current tightest limit obtained with free neutrons.

1. Introduction

The extremely successful Standard Model (SM) of particle physics provides testable experimental predictions usually agreeing with laboratory measurements and astronomical observations at the highest levels of accuracy [1, 2]. It is therefore considered as the best theory to describe the fundamental building blocks of the Universe at current measurement sensitivities. However, together with the Cosmological Standard

Model, it leaves some phenomena unexplained, e.g. the observed matter-antimatter imbalance also known as baryon asymmetry of the Universe (BAU) or the nature of dark matter (DM) and dark energy [3].

In the 1967 seminal article ‘Violation of CP invariance, C asymmetry, and baryon asymmetry of the Universe’ by A. Sakharov, the violation of the combined symmetry of charge conjugation and parity (CP) is identified as one of the three necessary criteria for the creation of the observed BAU [4] from initial symmetric conditions. In the SM, CP violation (CPV) may occur in the weak and the strong sectors. In the weak sector, it appears in the complex phase of the Cabibbo–Kobayashi–Maskawa [5] or the Pontecorvo–Maki–Nakagawa–Sakata [6] matrices describing the mixing of quarks or leptons in their mass and flavor states, respectively. In the quark sector, CPV has been observed and precisely measured in kaon [7–10] and B -meson [11, 12] decays. Although the CPV phase of the CKM matrix is nearly maximal [13], it is insufficient to generate the observed BAU [14].

In the strong sector, CPV appears as vacuum polarization term in the Lagrangian of quantum chromodynamics (QCDs) [15, 16], giving rise to an electric dipole moment (EDM) of the neutron on the order of $\bar{\theta} \times 10^{-16}$ e · cm, where $\bar{\theta}$ can take any value between 0 and 2π . Nevertheless, non-observation of a neutron EDM constrains the CP -violating phase in the strong interaction to a value that is particularly small, $\bar{\theta} < 10^{-10}$, constituting a puzzle known as the strong CP -problem [17].

A possible solution to the strong CP -problem was proposed by Peccei and Quinn in 1977 by introducing an additional chiral $U(1)_{PQ}$ symmetry [18, 19]. The spontaneous breaking of this symmetry results in a pseudo-Goldstone boson [17] to which one often refers to as the ‘canonical QCD axion.’ In 1984, Moody and Wilczek [20] proposed to search for a new, short-range, spin-dependent (SRSD) interaction, which could be mediated by very light, weakly coupled, spin-0 bosons, similar to the canonical axion. For spin-0 bosons, only two options exist to couple to fermions, either via a scalar or a pseudoscalar vertex with the coupling constants g_s and g_p , respectively. For a fermion-fermion interaction with only one boson exchange, the scalar and the pseudoscalar vertices permit three distinct interactions with (monopole)², (dipole)², or monopole–dipole virtual boson fields, involving g_s^2 , g_p^2 , or $g_s g_p$, respectively. One prominent candidate for the mediator particle of these (monopole)², (dipole)², and monopole-dipole interactions is the canonical axion, but may be other hypothetical bosons [21, 22], such as spin-0 axion-like particles (ALPs), which have similar properties to the canonical axion, or very light spin-1 bosons [23, 24] coupling via the vector (g_v) and the axial-vector (g_A) vertices. These low-mass particles, which couple very weakly to visible matter, are often referred to as weakly interacting sub-eV/slim particles (WISPs) [25].

The canonical QCD axion and additional ALPs are predicted in many BSM theories including super-symmetric extensions and string theory. They are considered promising candidates as microscopic constituents of DM [26, 27]. For the canonical axion, their allowed mass range is 10^{-13} – 10^{-2} eV, constrained by an assumption on the Peccei–Quinn symmetry breaking scale (lower bound) and stellar evolution arguments (upper bound) [28], and the original Peccei–Quinn symmetry sets a fixed relation between its mass and its coupling to the SM particles. On the contrary, there is no *a priori* relation between mass and coupling strength for ALPs, making the potential parameter space broader [28, 29]. Many experiments worldwide are actively searching for these particles using resonant cavity haloscopes [30, 31] or large-scale helioscopes [32] to detect WISPs based on cosmological and astrophysical sources. Additionally, laboratory-based experiments employing nuclear magnetic resonant precision magnetometers searching for EDM interactions with ALPs [33, 34], a broadband/resonant approach with a toroidal magnet looking for an axion-induced magnetic field [35], or employing search methods based on the concept of ‘light shining through a wall’ [36, 37] or the search for a ‘fifth force’ [38, 39], have also been looking for WISPs in the past few decades. To date, no evidence of the canonical QCD axion or any ALPs has been observed.

1.1. The monopole–dipole interaction

Among the three interactions, the monopole–dipole interaction involving $g_s g_p$ and violating P and T symmetries as well as combined CP symmetry, is of particular interest, as the demonstration of CPV would provide an evidence to one of the three essential criteria to explain the BAU [4]. The potential generated by the monopole–dipole interaction between a polarized (\dagger) and an unpolarized particle can be written as [20, 40]

$$V(r) = g_s g_p^\dagger \frac{\hbar^2}{8\pi m^\dagger} (\boldsymbol{\sigma}^\dagger \cdot \hat{\mathbf{r}}) \left(\frac{1}{r\lambda} + \frac{1}{r^2} \right) e^{-r/\lambda}, \quad (1)$$

where m^\dagger and $\boldsymbol{\sigma}^\dagger$ are the mass and the Pauli matrices belonging to the spin of the polarized particle, $\hat{\mathbf{r}}$ is the unit vector along the distance r between the particles, $\lambda = \hbar / (m^\dagger c)$ is the interaction range, and \hbar is the reduced Planck’s constant. The unpolarized and the polarized particles couple to the spin-0 boson via unitless scalar and pseudoscalar coupling constants g_s and g_p^\dagger , respectively.

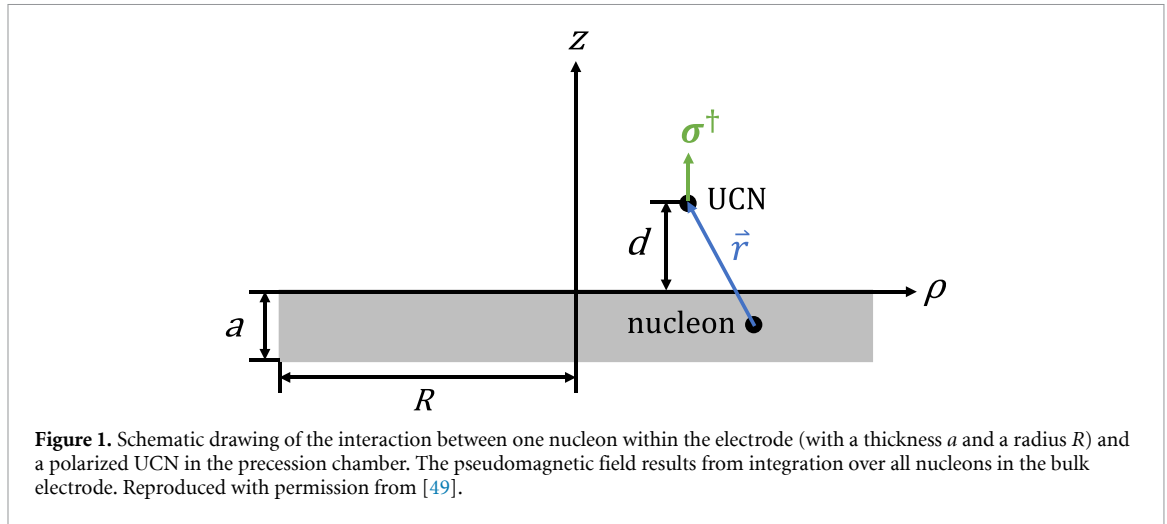


Figure 1. Schematic drawing of the interaction between one nucleon within the electrode (with a thickness a and a radius R) and a polarized UCN in the precession chamber. The pseudomagnetic field results from integration over all nucleons in the bulk electrode. Reproduced with permission from [49].

In [40, 41], it was proposed that ultracold neutrons (UCNs) can be used to search for ALPs. We searched for such an interaction with the apparatus originally built for the search for the EDM of the neutron (nEDM) [42], and with which we also set limits for an oscillating nEDM [43] through the axion-gluon coupling and for neutron to mirror-neutron oscillations [44] at the UCN source [45, 46] of the Paul Scherrer Institute (PSI) in Switzerland. In the experiment, polarized UCNs and polarized ^{199}Hg atoms populated a vacuum volume between two horizontal electrodes and an insulator ring. A sketch of the experimental apparatus is shown in figure 2, and details about the spectrometer and the measurement procedure are described in section 2. The SRSD interaction would involve the polarized UCNs stored in the vessel and unpolarized nucleons (protons and neutrons) on the electrode surfaces. The measurements were performed by comparing the Larmor precession frequencies of stored UCNs and ^{199}Hg atoms, which served as a cohabiting magnetometer, in a constant magnetic field \vec{B}_0 . An ALP-mediated SRSD interaction between vessel materials and trapped particles can be considered as a pseudomagnetic field b_{UCN}^* influencing the precession frequency of UCNs, whereas the effect on the ^{199}Hg atoms is negligible as their mass is much larger ($V(\mathbf{r}) \propto 1/m^\dagger$ in equation (1)). Hence, the ratio of the spin precession frequencies of UCNs and ^{199}Hg atoms,

$$\mathcal{R}^{\uparrow/\downarrow} = \left(\frac{f_n}{f_{\text{Hg}}} \right)^{\uparrow/\downarrow} = \left| \frac{\gamma_n}{\gamma_{\text{Hg}}} \right| \left(1 \pm \frac{b_{\text{UCN}}^*}{|\vec{B}_0|} \pm \frac{G_{\text{grav}} \langle z \rangle}{|\vec{B}_0|} + \delta_{\text{else}} \right), \quad (2)$$

is sensitive to this interaction while magnetic-field changes cancel and other effects corrected for. Here, γ_n and γ_{Hg} are the gyromagnetic ratios of the neutron and the ^{199}Hg , respectively, b_{UCN}^* is the pseudomagnetic field that would be experienced by UCNs stored in the apparatus (derived in section 1.2), and the $+/-$ signs correspond to the upward/downward directions of the magnetic field according to gravity. By measuring \mathcal{R} in opposite directions of \vec{B}_0 , the magnitude of the pseudomagnetic field can be extracted

$$b_{\text{UCN}}^* = \frac{\mathcal{R}^\uparrow - \mathcal{R}^\downarrow}{\mathcal{R}^\uparrow + \mathcal{R}^\downarrow} |\vec{B}_0|, \quad (3)$$

and in turn the strength of the interaction $g_s g_p$ can be deduced. The dominant systematic effect is due to the vertical center-of-mass offset (z) between the ^{199}Hg atoms and the UCNs in the presence of an effective magnetic-field gradient G_{grav} [47]. Additional effects δ_{else} are described in more detail below.

1.2. Derivation of the pseudomagnetic field

The interaction is described by the potential given in equation (1), and the effective interaction generated by one electrode in the apparatus is derived by integrating over all nucleons from the bulk matter. The corresponding pseudomagnetic field normal to the electrode surface at a height d is written as [48]

$$b^*(d) \approx g_s g_p^\dagger \frac{\hbar N \lambda}{2 \gamma^\dagger m^\dagger} \left(1 - e^{-a/\lambda} \right) e^{-d/\lambda}, \quad (4)$$

where γ^\dagger is the gyromagnetic ratio of the polarized particle, N is the nucleon density depending on the material of the electrode, and a is the electrode thickness, illustrated schematically in figure 1.

In the nEDM apparatus, both the top and the bottom electrodes made of aluminum contributed to this interaction in opposite directions, pointing from the electrodes to the UCNs stored in the chamber. We defined $z = 0$ at the center of the precession chamber such that the surfaces of the top and the bottom electrodes were at $z = +H/2$ and $z = -H/2$, respectively, where $H = 12$ cm is the chamber height. The total pseudomagnetic field measured at a vertical coordinate z can be written by summing up contributions from both electrodes using equation (4) as

$$b_{\text{ALP}}^*(z) = g_s g_p^\dagger \frac{\hbar \lambda}{2\gamma^\dagger m^\dagger} \left(1 - e^{-a/\lambda}\right) \left(N_{\text{bot}} e^{-(z+H/2)/\lambda} - N_{\text{top}} e^{-(H/2-z)/\lambda}\right), \quad (5)$$

where N_{bot} and N_{top} are the nucleon densities of the bottom and the top electrodes, respectively.

Since the UCNs have very low kinetic energies, their trajectories are strongly influenced by gravity. As a result, they were not uniformly distributed within the precession chamber; instead, the center of mass of the UCNs was shifted to negative z values. This effectively resulted in a center-of-mass offset $\langle z \rangle = -3.9(3)$ mm [42] with respect to that of the cohabiting ^{199}Hg atoms. A linear approximation of the normalized vertical-UCN-density function is given as [48]

$$\rho_n(z) = \frac{1}{H} \left(1 + \frac{12\langle z \rangle}{H^2} z\right). \quad (6)$$

The setup was sensitive to interactions of short ranges, approximately from μm to mm, a similar range as in [48, 50]; therefore, the UCN-density distribution can be simplified to a constant density at distances close to the surfaces of the electrodes, $\rho_n(-H/2)$ and $\rho_n(+H/2)$ [48]. The effective pseudomagnetic field, defined as pointing upwards with respect to gravity, experienced by all UCNs within the precession chamber, is solved analytically by integrating over the chamber height

$$\begin{aligned} b_{\text{UCN}}^* &= \int_{-H/2}^{+H/2} b_{\text{ALP}}^*(z) \rho_n(z) dz \\ &= g_s g_p^\dagger \frac{\hbar \lambda}{2\gamma^\dagger m^\dagger} \left(1 - e^{-a/\lambda}\right) \int_{-H/2}^{+H/2} \left[N_{\text{bot}} \rho_n\left(\frac{-H}{2}\right) e^{-(z+H/2)/\lambda} - N_{\text{top}} \rho_n\left(\frac{+H}{2}\right) e^{-(H/2-z)/\lambda} \right] dz \quad (7) \\ &= g_s g_p^\dagger \frac{\hbar \lambda^2}{2\gamma^\dagger m^\dagger H^2} \left[H(N_{\text{bot}} - N_{\text{top}}) - 6\langle z \rangle (N_{\text{bot}} + N_{\text{top}}) \right] \left(1 - e^{-a/\lambda}\right) \left(1 - e^{-H/\lambda}\right), \end{aligned}$$

where the top and the bottom electrodes contribute in opposite directions.

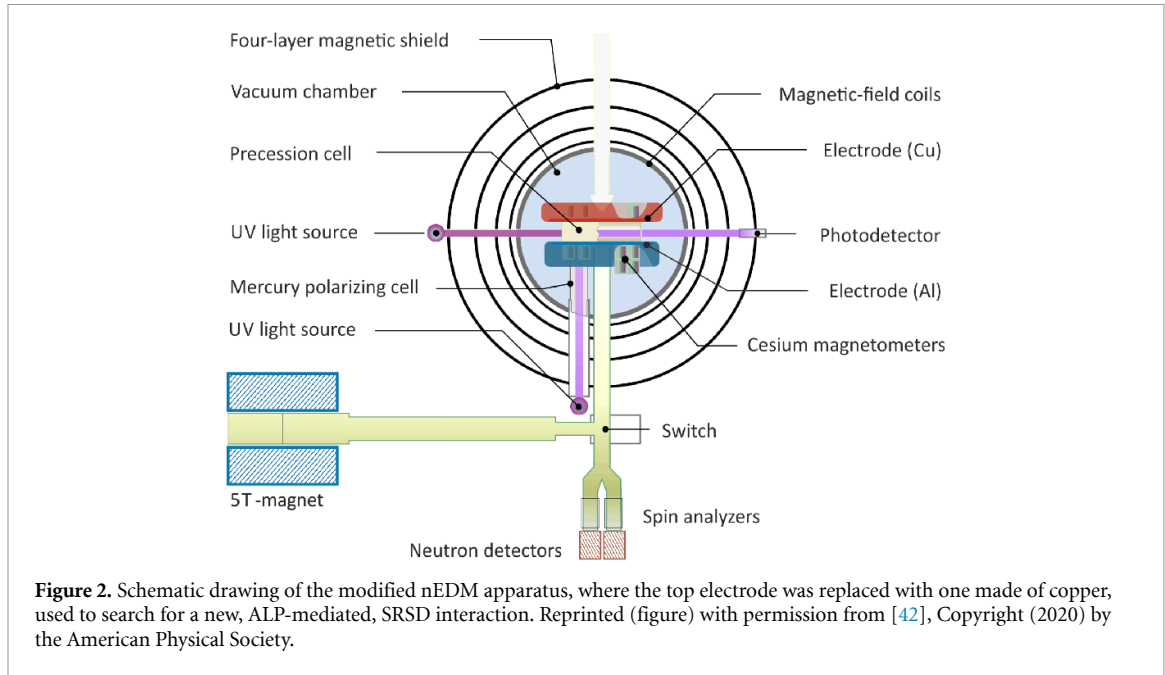
2. Measurement with the nEDM spectrometer

For the measurement, we exchanged the top electrode of the nEDM spectrometer by one made out of copper to increase the nucleon density, which increased the sensitivity to this interaction. A sketch of the modified apparatus is shown in figure 2, where no electric field was applied during these measurements. The nucleon density¹⁷ for the top electrode was $N_{\text{top}} = N_{\text{Cu}} = 5.40 \times 10^{30} \text{ m}^{-3}$, whereas the bottom electrode made of aluminum remained, with $N_{\text{bot}} = N_{\text{Al}} = 1.63 \times 10^{30} \text{ m}^{-3}$. In this way, an asymmetric pseudomagnetic field b_{ALP}^* was generated, increasing the sensitivity by a factor of 7.7 compared to that using both electrodes made of aluminum.

Further, we exchanged the ultraviolet light source of the probe beam of the ^{199}Hg -comagnetometer (HgM) from a mercury discharge lamp [52] to a locked frequency quadrupled diode laser¹⁸ with a wavelength of 253.7 nm [53] to maximize the sensitivity of the HgM readout. The rest of the apparatus remained unchanged compared to our previous search for an SRSD interaction mediated by an ALP [48]. Polarized mercury vapor and polarized UCNs precessed in a cylindrical storage chamber of $H = 12$ cm height. Its side walls were made of normal polystyrene with a radius of $R = 23.5$ cm, and the inside was coated with deuterated polystyrene [54]. The bottom was closed off by an aluminum electrode with a central shutter for UCNs and a smaller shutter for mercury vapor. All inner metal surfaces of the storage cylinder, including the aluminum and the copper electrode surfaces, were coated with a thin layer ($\sim 1\text{--}3 \mu\text{m}$ thickness) of diamond-like carbon [55, 56] to improve the coherence and storage times of UCNs and ^{199}Hg

¹⁷ The nucleon densities were calculated using the material densities and the atomic masses obtained from MaTeck's periodic table of elements (<https://mateck.com/en/>, accessed 26 February 2023) and [51].

¹⁸ TOPTICA Photonics AG. Product description TA / FA-FHG pro. Accessed 11 January 2022. <http://www.toptica.com/products/tunable-diode-lasers/frequency-converted-lasers/ta-fhg-pro/>.



atoms. Additionally, a total of 15 cesium magnetometers (CsM), of which seven were installed above and eight below the precession chamber, were used to monitor the magnetic-field gradient G_{grav} along the chamber axis [57]. A cosine-theta coil comprising around 50 turns powered with a current of about 17 mA created a stable and uniform magnetic field of $|\vec{B}_0| \approx \pm 1036$ nT vertically across the chamber. Additionally, 30 trimcoils were installed around the vacuum chamber that could be used to create a certain magnetic-field configuration if required. Four layers of cylindrical mu-metal shield and a surrounding field compensation coil system [58] were used to passively and actively improve the stability of the magnetic field.

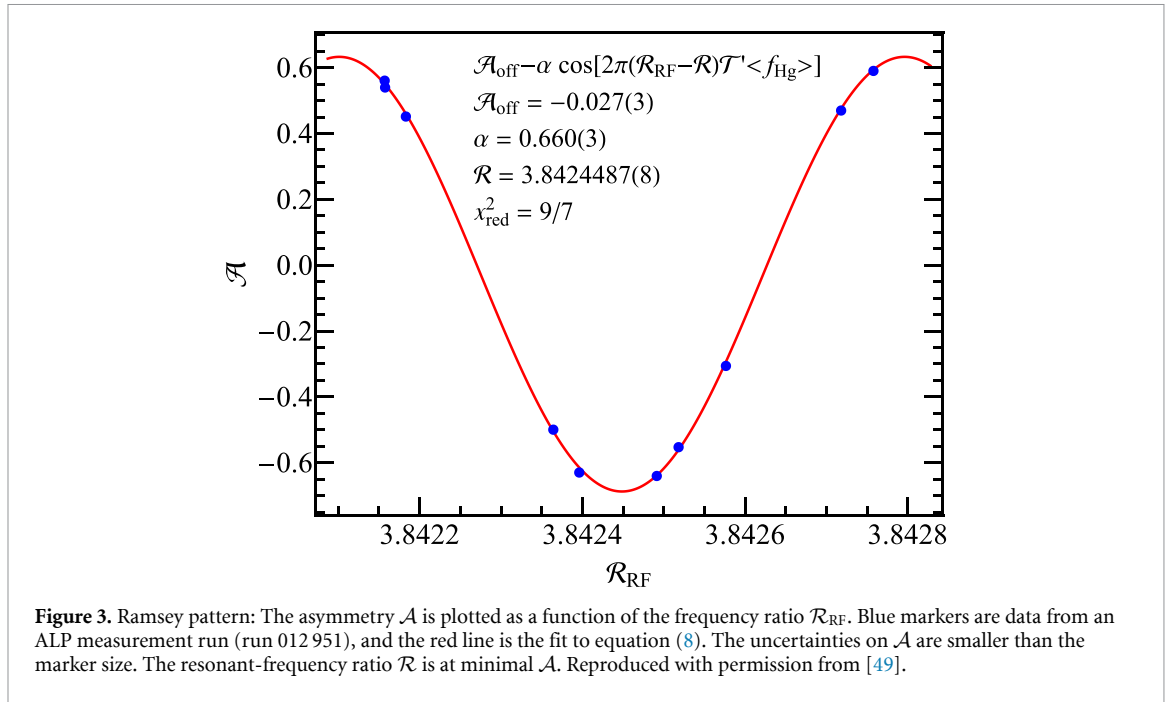
In each measurement *cycle*, polarized UCNs in the magnetic field \vec{B}_0 were used for Ramsey's method of separated oscillatory fields [59]. A cycle started by bringing the polarized UCNs into the precession chamber, followed by the filling of the polarized ^{199}Hg atoms. When both particle species were prepared in their initial stages in the storage chamber, two low-frequency pulses were applied consecutively to the ^{199}Hg atoms and to the UCNs to flip their spins to the transverse plane. These pulses are called $\pi/2$ -pulses. After a free-spin-precession duration of $\mathcal{T} = 180$ s, a second $\pi/2$ -pulse, in phase with the first one, was applied to the UCNs to further tip their spins for another $\pi/2$. Afterwards, a spin-sensitive detection system [60, 61] counted neutrons in spin-up (N^\uparrow) and spin-down (N^\downarrow) states at the end of the cycle, from which the asymmetry $\mathcal{A} = (N^\uparrow - N^\downarrow) / (N^\uparrow + N^\downarrow)$ was calculated. The HgM precession frequency was measured using a circularly polarized, resonant ultraviolet laser beam at 253.7 nm wavelength, traversing the chamber while recording the spin-precession-modulated light intensity with a photo-multiplier tube [53]. A measurement *run* consisted of approximately ten cycles with different spin-flipping frequencies $f_{n,\text{RF}}$. These frequencies that were applied as $\pi/2$ -pulses were slightly detuned from the resonant f_n . The scan of $f_{n,\text{RF}}$ throughout every run led to different asymmetries of the final-state neutrons in each cycle. In combination with the measured HgM frequency of a single cycle, an interference pattern, *Ramsey pattern*, may be plotted by displaying the asymmetry as a function of the frequency ratio $\mathcal{R}_{\text{RF}} = f_{n,\text{RF}}/f_{\text{Hg}}$ (figure 3).

The central Ramsey fringe, approximated well with a cosine function,

$$\mathcal{A} = \mathcal{A}_{\text{off}} - \alpha \cos [2\pi (\mathcal{R}_{\text{RF}} - \mathcal{R}) \mathcal{T}' \langle f_{\text{Hg}} \rangle], \quad (8)$$

was fitted to the interference pattern, where $\langle f_{\text{Hg}} \rangle$ is the average HgM frequency of all cycles within the run. Three parameters, the asymmetry offset \mathcal{A}_{off} , the visibility (or *Ramsey contrast*) α , and the resonant-frequency ratio $\mathcal{R} = f_n/f_{\text{Hg}}$, were extracted. $\mathcal{T}' = \mathcal{T} + 4\tau_n/\pi$ is the effective time related to the fringe width, where $\tau_n = 2$ s is the length of a neutron $\pi/2$ -pulse. By taking the ratio of the two frequencies, we compensated for magnetic-field changes from one cycle to the next one, which cancel in equation (2).

The difference of resonant-frequency ratios \mathcal{R} , taken for direction-inverted magnetic-field configurations permits the extraction of b_{UCN}^* using equation (3). As \mathcal{R} is a linear function of G_{grav} (equation (2)), we intentionally took data at different vertical magnetic-field gradients. Each measurement run thus comprised a certain magnetic-field configuration. The vertical magnetic-field gradient was generated by applying dedicated currents in a pair of trim coils installed above and below the vacuum



tank [62]. In addition to the high-granularity maps of the magnetic field, taken using a dedicated measurement device [63], the spatial distribution of the magnetic field was measured continuously with a sampling rate of 1 Hz with 15 CsM. Using a linear fit of G_{grav} versus \mathcal{R} (G_{grav}) by correcting for all known systematic effects of \mathcal{R} (section 3.1) and precisely determining G_{grav} (section 3.2), \mathcal{R}_0^\uparrow and \mathcal{R}_0^\downarrow , resonant-frequency ratios at $G_{\text{grav}} = 0$ for both \vec{B}_0 directions, were precisely determined (section 3.3).

3. Data analysis

3.1. Extraction of the resonant-frequency ratio \mathcal{R}

For each measurement run, a resonant \mathcal{R} was obtained by fitting the Ramsey pattern, equation (8). Various statistical uncertainties and systematic effects influenced the measurement of \mathcal{R} . Four effects were considered for each measurement cycle as stochastic uncertainties. These include the neutron counting statistics, the uncertainty of the estimated HgM frequency, the magnetic-field-gradient (G_{grav}) drift between cycles, and the Ramsey–Bloch–Siegert shift [64, 65] induced by the $\pi/2$ -pulse of the HgM onto the neutron spin. The last effect resulted from the fact that the circularly rotating magnetic field applied to the ^{199}Hg atoms resulted in small random tilts of the neutron spins. Each effect resulted in an uncertainty on the measured asymmetry \mathcal{A} , which was further propagated to the uncertainty of \mathcal{R} according to equation (8) using the fitted values for α and \mathcal{R} . Table 1 shows the average uncertainties of each effect for all measurement cycles. We calculated the reduced chi-square χ_{red}^2 from the Ramsey fit for all 17 runs including both directions of \vec{B}_0 , and the mean value was 9.15. Assuming pure Poisson statistics, the reduced chi-square χ_{red}^2 should be approximately 1. A scaling factor of 2.8, the square-root of the average χ_{red}^2 values excluding one run with $\chi_{\text{red}}^2 > 20$, was applied to the \mathcal{R} errors obtained from the fit of all runs to account for stochastic errors that were unaccounted for¹⁹.

We recall that the dominant systematic effect is the gravitational shift δ_{grav} resulting from the center-of-mass offset $\langle z \rangle$ between the UCN and the ^{199}Hg ensembles (equation (2)). In the presence of a vertical magnetic-field gradient G_{grav} , both species measure slightly different volume averages of the magnetic field. The gravitational shift is calculated as

$$\delta_{\text{grav}} = \frac{\langle B_z \rangle_{\text{n}}}{\langle B_z \rangle_{\text{Hg}}} - 1 = \pm \frac{G_{\text{grav}} \langle z \rangle}{|\vec{B}_0|}, \quad (9)$$

¹⁹ The reason of excluding this run was due to the fact that its χ_{red}^2 was almost two times larger than the second largest χ_{red}^2 among all 17 runs. However, this run was still included in the final analysis. We verified that by excluding this specific run, the final result remained unchanged.

Table 1. Stochastic uncertainties of \mathcal{R} from all measurement cycles. The total numbers of neutrons have mean values of approximately 14 000 and 10 000 for the magnetic field pointing upwards and downwards, respectively.

Effect / 1×10^{-7}	B_0 up	B_0 down
Neutron counts	1.84	2.26
HgM frequency	0.75	0.69
Gradient drift	0.02	0.02
^{199}Hg spin-flip pulse	0.07	0.23
Total stochastic effects	2.02	2.41

where

$$G_{\text{grav}} = G_{1,0} + G_{3,0} \left(\frac{3H^2}{20} - \frac{3R^2}{4} \right) + G_{5,0} \left(\frac{5R^4}{8} - \frac{3R^2H^2}{8} + \frac{3H^4}{112} \right) \quad (10)$$

is the effective magnetic-field gradient parallel to the gravitational gradient calculated using a polynomial expansion of the magnetic field to fifth degree [63, 66]. $G_{\ell,m}$ are expansion coefficients of degree l and order m of the harmonic polynomial, whereas $H = 12$ cm and $R = 23.5$ cm are the height and the radius of the precession chamber. The $+/-$ signs in equation (9) correspond to \vec{B}_0 in upward/downward directions, respectively, with $\langle z \rangle < 0$. More details on this effect is described in section 3.2.

Other known effects δ_{else} shown in equation (2) are summarized as

$$\delta_{\text{else}} = \delta_{\text{T}} + \delta_{\text{Earth}} + \delta_{\text{light}} + \delta_{\text{inc}} + \delta_{\text{JNN}}, \quad (11)$$

which are caused by the transverse magnetic-field components, the rotation of Earth, the UV laser beam for the HgM readout, the incoherent scattering of UCNs on the ^{199}Hg atoms, and magnetic-field fluctuations resulting from Johnson–Nyquist noise (JNN) [67, 68], respectively. They may be divided into two categories. On the one hand, constant shifts of the UCN or HgM frequency lead to a deviation of \mathcal{R} from the ratio of pure gyromagnetic ratios. These include the first three effects, δ_{T} , δ_{Earth} , and δ_{light} . On the other hand, δ_{inc} and δ_{JNN} are pure stochastic effects, which do not shift the mean \mathcal{R} value, but result in an increase of the measurement uncertainty. These effects are shown in section 3.3.

The transverse shift δ_{T} is a consequence of transverse components of the magnetic field B_{T} . UCNs in a magnetic field of $1 \mu\text{T}$ sample the field in the adiabatic regime of slow particles in a high magnetic field. The measured mean frequency $\omega_{\text{n}} = \gamma_{\text{n}} \sqrt{\langle B_x^2 + B_y^2 + B_z^2 \rangle}$ is proportional to the volume average of the magnetic-field modulus. By contrast, ^{199}Hg atoms in the same magnetic field fall into the nonadiabatic regime of fast particles in a low magnetic field, such that their spins precess at a mean frequency $\omega_{\text{Hg}} = \gamma_{\text{Hg}} \sqrt{\langle B_x \rangle^2 + \langle B_y \rangle^2 + \langle B_z \rangle^2}$ given by the volume average of the vector magnetic field. In the presence of B_{T} , this results in

$$\delta_{\text{T}} = \frac{\langle B_{\text{T}}^2 \rangle}{2\vec{B}_0^2}, \quad (12)$$

with

$$\langle B_{\text{T}}^2 \rangle = \langle \Delta B_x^2 + \Delta B_y^2 \rangle \quad (13)$$

being the mean-square transverse magnetic-field components, where $\Delta B_x = B_x - \langle B_x \rangle$ and $\Delta B_y = B_y - \langle B_y \rangle$. For each run, i.e. one magnetic-field configuration, we calculated $\langle B_{\text{T}}^2 \rangle$ using the field maps [63] and corrected the resonant \mathcal{R} value obtained from the Ramsey fit (equation (8)) by δ_{T} .

Effectively, given the rotation of Earth, the precession frequencies of UCNs and ^{199}Hg atoms are measured in a rotating frame of reference. They are a combination of the Larmor frequency in a stationary frame and the Earth's rotational frequency, $f_{\text{Earth}} = 11.6 \mu\text{Hz}$. The associated shift in \mathcal{R} was corrected for by calculating

$$\delta_{\text{Earth}} = \mp \left(\frac{f_{\text{Earth}}}{f_{\text{n}}} + \frac{f_{\text{Earth}}}{f_{\text{Hg}}} \right) \cos(\theta_{\text{PSI}}) = \mp 1.4 \times 10^{-6}, \quad (14)$$

where $\cos(\theta_{\text{PSI}}) = 0.738$ is the cosine of the angle between the \vec{B}_0 direction and the rotational axis of the Earth, corresponding to the latitude of the PSI, and the $-/+$ signs correspond to the upward/downward directions of \vec{B}_0 , respectively.

The third effect δ_{light} is related to the UV laser traversing the precession chamber to read out the HgM signal. This value was not quantified during the measurement; therefore, we only estimate its effect and consider it as another contribution to the final uncertainty of \mathcal{R} . Details are given in section 3.3.

3.2. Determination of the vertical magnetic-field gradient G_{grav}

A total of 15 CsM, which were of scalar-type magnetometers, measured the magnitudes of the magnetic field above and below the precession chamber during a measurement, which was used to quantify G_{grav} . Because of the applied $\vec{B}_0 \approx 1 \mu\text{T} \hat{e}_z$, the transverse fields of order 1 nT were negligible compared to the vertical field; hence, the scalar fields measured by the CsM were the effective vertical-field component B_z .

The magnetic fields measured by the CsM were described by a polynomial expansion [66]. The gradients $G_{\ell,m}$ were extracted by fitting the 15 field values measured by the CsM to the z component of the polynomial expansion

$$B_{\text{CsM}}^i(\mathbf{r}^i) = \sum_{\ell,m} G_{\ell,m} \Pi_{z,\ell,m}(\mathbf{r}^i), \quad (15)$$

where $i = 1, 2, \dots, 15$ is the index of the CsM, \mathbf{r}^i is the position of the corresponding CsM, and $\Pi_{z,\ell,m}$ is a function (or mode) expanded in harmonic polynomials of degree ℓ and order m depending on \mathbf{r}^i .

For each degree ℓ , the order m runs from $-\ell$ to $+\ell$ for $\Pi_{z,\ell,m}$, which gives $(2\ell + 1)$ terms. It was observed that lower-degree fields were subjected to fluctuations; thus, they were measured online with CsM. Constrained by the number of 15 CsM, the highest full parametrization one can achieve with this method is of second-degree, which contains nine free parameters. The contributions of higher-degree fields were found to be more stable and reproducible. To resolve the problem of higher-degree fields that were not taken into account, we combined both online CsM measurements and offline field maps [63] to achieve an improved estimate of G_{grav} . With the field maps, the magnetic fields could be expanded up to sixth degree for all three components in x , y , and z . The expression of G_{grav} could thus be expanded to fifth degree (equation (10)). Note that only odd gradients contribute to G_{grav} as the average-magnetic-field components given by even gradients cancel out for ^{199}Hg atoms and UCNs.

Several methods to combine cycle-by-cycle CsM data with magnetic-field maps were investigated using synthesized magnetic-field readings, which worked as follows. We calculated field values at the CsM positions using the magnetic-field-map data and varying the coefficients $G_{\ell,m}^{\text{syn}}$ randomly using a Gaussian distribution (equation (17)). In addition, a uniformly distributed random offset in the range of ± 120 pT [57] was added at each CsM location, accounting for possible sensor offsets. In total, 200 random fields were synthesized and analyzed using eight different methods [49]. The optimal method was selected by minimizing the difference between the synthesized and the fitted G_{grav} up to fifth degree using equation (10),

$$\Delta G_{\text{grav}} = G_{\text{grav}}^{\text{syn}} - G_{\text{grav}}^{\text{fit}}, \quad (16)$$

referred to as the deviation. Each synthesized gradient composing $G_{\text{grav}}^{\text{syn}}$ included a random error drawn from a Gaussian distribution, whose standard deviation was the uncertainty of the map, and was given as

$$G_{\ell,m}^{\text{syn}} = G_{\ell,m}^{\text{map}} + \delta_{G_{\ell,m}}^{\text{map}}. \quad (17)$$

The uncertainty of the fitted gradient $\sigma_{G_{\text{grav}}}$ was calculated with error propagation from each gradient-fit error $\sigma_{G_{1,0}}^{\text{fit}}$, $\sigma_{G_{3,0}}^{\text{fit}}$, and $\sigma_{G_{5,0}}^{\text{fit}}$ in equation (10).

We concluded that the optimal method was achieved by removing the fields described by higher-degree harmonic polynomials with $\ell = 3, \dots, 6$ using the map gradients and performing a second-degree fit including nine gradients up to $\ell = 2$ to the residual fields. The optimal fit method, even in the presence of CsM offsets with a standard deviation as large as $\sigma_{B_{\text{offset}}} = 115$ pT, estimated the coefficients with a deviation in the range of $|\Delta G_{\text{grav}}| \sim 2\text{--}3$ pT cm^{-1} , and with fit uncertainties of $\sigma_{G_{\text{grav}}} < 3.8$ pT cm^{-1} (upward \vec{B}_0) and $\sigma_{G_{\text{grav}}} < 4.5$ pT cm^{-1} (downward \vec{B}_0).

This method was applied to all 17 runs of data, consisting of a total of 170 cycles. The residuals $\Delta B^i = B_{\text{low}}^i - B_{\text{fit}}^i$ for each CsM i in each cycle was calculated, where B_{low}^i are the field values used in the fit to the polynomial expansion up to second degree after removing higher-degree contributions, and B_{fit}^i are the calculated values at each CsM position using the fitted gradients. All ΔB^i were < 250 pT, which were below the uncertainties of the field maps. For each cycle, G_{grav} was calculated using the expansion up to fifth degree, where $G_{1,0}$ was obtained from the second-degree-polynomial fit, and $G_{3,0}$ as well as $G_{5,0}$ were taken from the map values. The average value of the estimated G_{grav} from all cycles in a run was taken as the vertical gradient of this magnetic-field configuration.

To correct for potential systematic effects on the calculated effective gradient G_{grav} , we made use of the *visibility parabola*, which is the visibility of the Ramsey fringe α plotted as a function of G_{grav} . The parabola reaches its maximum at the minimum vertical magnetic-field gradient, where gravitationally enhanced

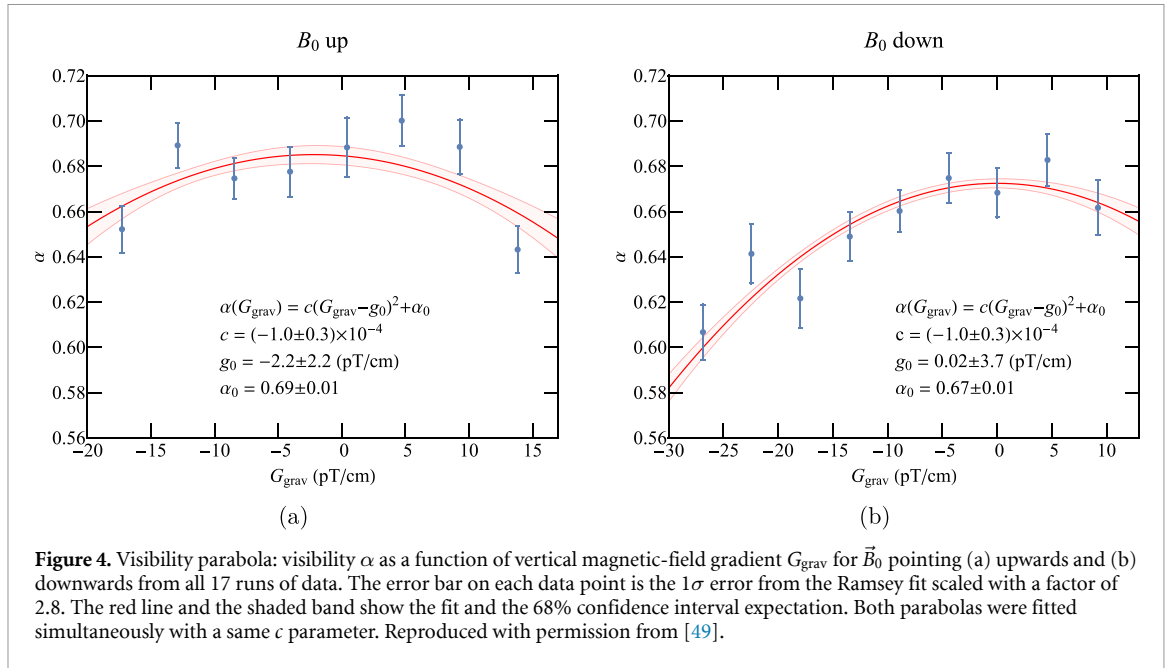


Figure 4. Visibility parabola: visibility α as a function of vertical magnetic-field gradient G_{grav} for \vec{B}_0 pointing (a) upwards and (b) downwards from all 17 runs of data. The error bar on each data point is the 1σ error from the Ramsey fit scaled with a factor of 2.8. The red line and the shaded band show the fit and the 68% confidence interval expectation. Both parabolas were fitted simultaneously with a same c parameter. Reproduced with permission from [49].

depolarization [69, 70] is negligible. Figure 4 shows the parabola for \vec{B}_0 pointing upwards (figure 4(a)) and downwards (figure 4(b)) with both reaching a similar maximal visibility. The parabolas were fitted with a simple parabolic function $\alpha(G_{\text{grav}}) = c(G_{\text{grav}} - g_0)^2 + \alpha_0$, where g_0 is the expected zero gradient. The maximal visibilities were reached at $g_0^\uparrow = -2.2 \pm 2.2 \text{ pT cm}^{-1}$ and $g_0^\downarrow = 0.02 \pm 3.7 \text{ pT cm}^{-1}$ for the upward and the downward \vec{B}_0 directions, respectively. The uncertainties on the fitted parameters were estimated by scaling $\chi_{\text{red}}^2 = \chi^2/\text{d.o.f.}$ to 1 in each parabola fit. To account for this potential shift, we corrected the effective G_{grav} of each run with $g_0^\uparrow = -2.2 \text{ pT cm}^{-1}$ or $g_0^\downarrow = 0.02 \text{ pT cm}^{-1}$.

3.3. Crossing-point analysis

Figure 5 shows the \mathcal{R} values, after δ_T and δ_{Earth} corrections, as a function of the corrected G_{grav} (figure 4). Red upward triangles and blue downward triangles are runs with \vec{B}_0 pointing upwards and downwards, respectively. A linear fit to the data from all runs with both directions of \vec{B}_0 (+/- correspond to upward/downward) was applied to

$$\mathcal{R}^{\uparrow/\downarrow} = \mathcal{R}_0^{\uparrow/\downarrow} \left(1 \pm \frac{\langle z \rangle}{|\vec{B}_0|} G_{\text{grav}}^{\uparrow/\downarrow} \right) \quad (18)$$

simultaneously, sharing the parameter $\langle z \rangle$, while the $\mathcal{R}_0^{\uparrow/\downarrow}$ values were kept separate for both directions. This is the so-called crossing-point analysis. The best fit was obtained for

$$\begin{aligned} \mathcal{R}_0^\uparrow &= 3.8424563(08), \\ \mathcal{R}_0^\downarrow &= 3.8424622(12), \text{ and} \\ \langle z \rangle &= -0.43(2) \text{ cm}, \end{aligned} \quad (19)$$

with $\chi_{\text{red}}^2 = \chi^2/\text{d.o.f.} = 31.9/14$. The underestimated uncertainties caused χ_{red}^2 to be larger than 1. The uncertainties shown in equation (19) were corrected for this stochastic error. Compared to the total statistical errors shown in table 1 summing from all known effects, these are a factor of 4–5 larger, corresponding to our initial scaling factor of 2.8 multiplied by the correction factor $\sqrt{31.9/14}$. The center-of-mass offset $\langle z \rangle$ was in agreement with the values found in [42], $\langle z \rangle = -0.39(3) \text{ cm}$, and [66], $\langle z \rangle = -0.38(3) \text{ cm}$, and the crossing point was at $G_\times = -1.9(5) \text{ pT cm}^{-1}$.

In the following paragraphs, we distinguish two different kinds of uncertainties associated with \mathcal{R} as shown in equation (2). The first kind was systematic effects, leading to a bias, whereas the second kind was considered purely stochastic, only increasing the measurement uncertainty.

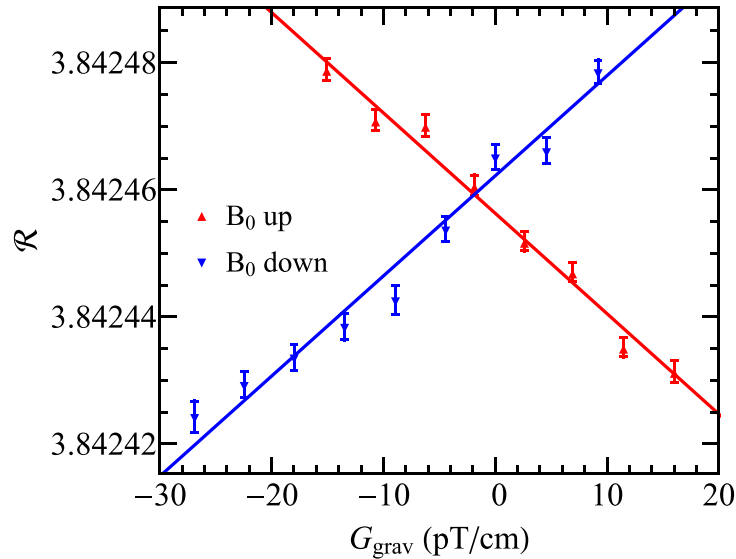


Figure 5. Frequency ratio \mathcal{R} as a function of vertical magnetic-field gradient G_{grav} for all runs with different field configurations. Red upward and blue downward triangles correspond to \vec{B}_0 pointing upwards and downwards, respectively. The error bar for each \mathcal{R} is the fit error from the Ramsey fit scaled by 2.8. The error of G_{grav} for each data point with an average value of 4.05 pT cm^{-1} over all 17 runs was not included in the error of \mathcal{R} individually. Instead, we considered this effect a global systematic uncertainty to all runs that resulted in an error contribution to both of the fitted $\mathcal{R}^{\uparrow/\downarrow}$ values. For this, the error obtained from each fit of the visibility parabolas was used (vertical magnetic-field gradient in table 2). Straight lines shown here were obtained using the best-fit values (equation (19)) in the fit equations (equation (18)). Reproduced with permission from [49].

The most important systematic effect of the first kind is the shift δ_{grav} induced by a vertical magnetic-field gradient. From the visibility parabolas (figure 4), $g_0^{\uparrow/\downarrow}$ were considered as systematic shifts on \mathcal{R} . For all runs, G_{grav} were corrected for with $g_0^{\uparrow/\downarrow}$, and the uncertainties of the fitted $g_0^{\uparrow/\downarrow}$ lead to

$$\begin{aligned}\sigma_{\mathcal{R}_{\text{grav}}}^{\uparrow} &= 35 \times 10^{-7} \text{ and} \\ \sigma_{\mathcal{R}_{\text{grav}}}^{\downarrow} &= 59 \times 10^{-7}.\end{aligned}\quad (20)$$

The second largest systematic effect δ_{T} arises from the residual transverse field. In addition to the shift in \mathcal{R} , corrected for run-by-run, an error on the mean-squared transverse field $\sigma_{\langle B_{\text{T}}^2 \rangle}$ was calculated making use of the concept of *reproducibility* of the field maps [63], quantifying the spread in measurements of identical magnetic-field configurations taken over several years. This results in shifts of

$$\begin{aligned}\mathcal{R}_{\text{T}}^{\uparrow} &= (7.3 \pm 4.7) \times 10^{-7} \text{ and} \\ \mathcal{R}_{\text{T}}^{\downarrow} &= (6.4 \pm 4.1) \times 10^{-7}.\end{aligned}\quad (21)$$

The third systematic shift δ_{light} may occur resulting from the resonant UV laser beam traversing the precession chamber to read out the ^{199}Hg spin precession. Two different systematic effects, the vector and the direct light shifts, were considered. The vector light shift was measured for our previous experiment [62] using a ^{204}Hg discharge lamp as the light source. This shift, which can be interpreted as the projection of the magnetic field of the photons traversing the precession chamber onto the \vec{B}_0 -field direction, is magnetic-field direction dependent. As we exchanged the slightly off-resonant ^{204}Hg lamp with a laser beam resonantly locked to the $^{199}\text{Hg } 6^1S_0 \rightarrow 6^3P_1 F = 1/2$ transition, the shift reduced by a factor of 7.7 [71] to

$$\begin{aligned}\mathcal{R}_{\text{VL}}^{\uparrow} &= (1.5 \pm 6.9) \times 10^{-7} \text{ and} \\ \mathcal{R}_{\text{VL}}^{\downarrow} &= (1.2 \pm 5.4) \times 10^{-7},\end{aligned}\quad (22)$$

where we kept the original uncertainties as the effect of the laser light power, which had an impact on the vector light shift, was not quantified. In addition, the direct light shift accounts for the fact that while the probed atom is in the $6^3P_1 F = 1/2$ state, the spin precesses at a different frequency. This will lead to a shift proportional to the light power and was estimated to be about 0.01 ppm [42] in the nEDM measurement with the same apparatus still using the ^{204}Hg discharge lamp. An increase in light power would also result in a decrease of the transverse depolarization time T_2 of the mercury precession, which was not observed.

Table 2. Error budget for the overall errors on \mathcal{R} resulting from statistics and from systematic effects for both \vec{B}_0 directions. Note that the effects resulting from the vertical magnetic-field gradient and the transverse magnetic field were taken into account before the fit for the crossing point analysis.

Effect / 1×10^{-7}	B_0 up	B_0 down
Statistics (uncertainty)	± 8	± 12
Vertical magnetic-field gradient	35 ± 35	-0.3 ± 59
Residual transverse field	7.3 ± 4.7	6.4 ± 4.1
Mercury light	1.9 ± 6.9	1.6 ± 5.5

Nevertheless, to account for a possible doubling of the light intensity because of the change to the resonant laser light, we estimate

$$\mathcal{R}_{\text{DL}}^{\uparrow/\downarrow} = (0.4 \pm 0.8) \times 10^{-7}. \quad (23)$$

The contributions from both the vector and the direct light shifts are summed together and shown as the effect from the mercury light in table 2.

Within the medium of spin-polarized ^{199}Hg vapor, UCNs are subjected to incoherent scattering on the ^{199}Hg nucleus, which can be described as a spin-dependent nuclear interaction. This acts as a pseudomagnetic field, which is proportional to the incoherent scattering length $|b_{\text{inc}}| = 15.5 \text{ fm}$ [72, 73]. For an imperfect $\pi/2$ -pulse of the HgM, a residual polarization along \vec{B}_0 creates a pseudomagnetic field, resulting in a frequency shift of UCNs and consequently a shift δ_{inc} of \mathcal{R} . We estimated the random fluctuation of ^{199}Hg polarization and quantified the resultant error on \mathcal{R} as $\sigma_{R_{\text{inc}}}^{\uparrow/\downarrow} \leq 5 \times 10^{-10}$. This effect is three orders of magnitude smaller than the light shift δ_{light} ; hence, we consider it negligible.

The precession of spin-polarized particles is affected by magnetic-field fluctuations resulting from JNN, originating from thermal motion of charge carriers inside the electrodes. Because of the difference between adiabatic and nonadiabatic magnetic-field samplings for UCNs and ^{199}Hg atoms, the volume-averaged fields sampled by both species are slightly different. A finite-element analysis was used to simulate temporal and spatial noise [74] from which we calculated the time-and-volume-averaged magnetic-field difference sensed by both particle ensembles. As JNN leads to random magnetic-field fluctuations independent of \vec{B}_0 polarity, we assume that this effect δ_{JNN} only increases the measurement uncertainty but does not shift the central \mathcal{R} value. The corresponding uncertainty was estimated to be $\sigma_{R_{\text{JNN}}}^{\uparrow/\downarrow} \leq 1 \times 10^{-9}$. As this effect is two orders of magnitude smaller than δ_{light} , we did not include it in the error budget.

The analysis of the measured data, including all shifts and uncertainties as listed in table 2, results in two independent \mathcal{R} values

$$\begin{aligned} \mathcal{R}^{\uparrow} &= 3.8424563(08)_{\text{stat}}(36)_{\text{sys}} \quad \text{and} \\ \mathcal{R}^{\downarrow} &= 3.8424622(12)_{\text{stat}}(59)_{\text{sys}} \end{aligned} \quad (24)$$

at the limit of $G_{\text{grav}} = 0$. Both values are in agreement with our previous measurement of the neutron to mercury gyromagnetic ratio [62],

$$\gamma_{\text{n}}/\gamma_{\text{Hg}} = 3.8424574(30). \quad (25)$$

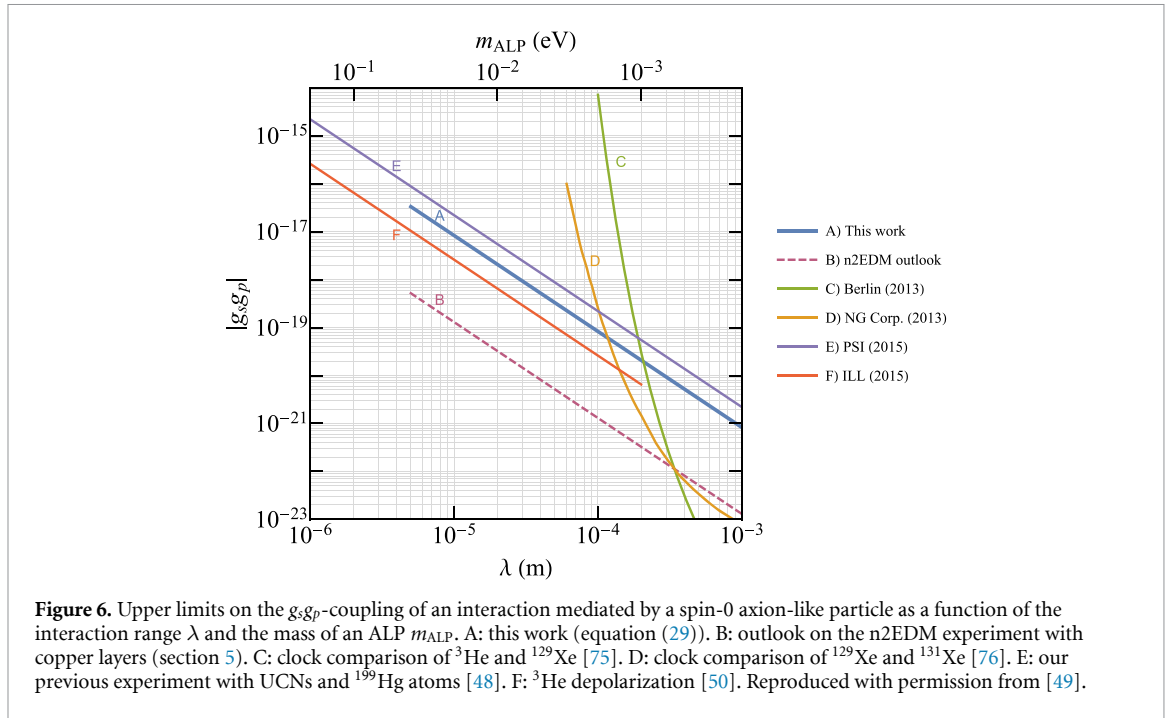
4. Interpretation of results

According to equation (2), b_{UCN}^* was extracted at the limit of $G_{\text{grav}} = 0$ after correcting for all systematic effects δ_{else} ,

$$b_{\text{UCN}}^* = \frac{\mathcal{R}^{\uparrow} - \mathcal{R}^{\downarrow}}{\mathcal{R}^{\uparrow} + \mathcal{R}^{\downarrow}} \left| \vec{B}_0 \right| = -0.80 \text{ pT}, \quad (26)$$

where $\left| \vec{B}_0 \right| = 1037.19(2) \text{ nT}$ was taken from the average \vec{B}_0 value of all runs. The uncertainty of b_{UCN}^* was calculated by including uncertainties from \mathcal{R}^{\uparrow} , \mathcal{R}^{\downarrow} , and \vec{B}_0 ,

$$\sigma_{b_{\text{UCN}}^*} = \left\{ \left[\frac{2\mathcal{R}^{\downarrow} \left| \vec{B}_0 \right|}{(\mathcal{R}^{\uparrow} + \mathcal{R}^{\downarrow})^2} \sigma_{\mathcal{R}^{\uparrow}} \right]^2 + \left[\frac{-2\mathcal{R}^{\uparrow} \left| \vec{B}_0 \right|}{(\mathcal{R}^{\uparrow} + \mathcal{R}^{\downarrow})^2} \sigma_{\mathcal{R}^{\downarrow}} \right]^2 + \left[\frac{\mathcal{R}^{\uparrow} - \mathcal{R}^{\downarrow}}{\mathcal{R}^{\uparrow} + \mathcal{R}^{\downarrow}} \sigma_{\vec{B}_0} \right]^2 \right\}^{1/2} = 0.96 \text{ pT}. \quad (27)$$



The errors $\sigma_{\mathcal{R}}^{\uparrow}$ and $\sigma_{\mathcal{R}}^{\downarrow}$ were calculated by summing in quadrature the statistical error and all systematic effects that contributed to the error budget of \mathcal{R} (table 2). $\sigma_{\vec{B}_0}$ was taken from the larger of the two standard deviations, $\sigma_{\vec{B}_0}^{\uparrow} = 17$ pT and $\sigma_{\vec{B}_0}^{\downarrow} = 22$ pT, measured within one \vec{B}_0 direction instead of taking the standard deviation of all 17 runs. Using equation (7), $g_s g_p$ was derived as

$$g_s g_p = b_{\text{UCN}}^* \frac{2\gamma_n m_n H^2}{\hbar \lambda^2 [H(N_{\text{bot}} - N_{\text{top}}) - 6\langle z \rangle (N_{\text{bot}} + N_{\text{top}})]} \left(1 - e^{-a/\lambda}\right)^{-1} \left(1 - e^{-H/\lambda}\right)^{-1}. \quad (28)$$

With the measured b_{UCN}^* (equation (26)) and the estimated error $\sigma_{b_{\text{UCN}}^*}$ (equation (27)), a 95% confidence level limit on $g_s g_p$ gives

$$g_s g_p \lambda^2 < 8.3 \times 10^{-28} \text{ m}^2, \quad (29)$$

for $5 \mu\text{m} < \lambda < 25$ mm. On the one hand, the upper limit of this range was defined as the thickness of the electrodes. Approaching the upper limit, the last two terms in equation (28) depart from 1, and the relation $g_s g_p \propto 1/\lambda^2$ is not fulfilled anymore, which reduces the measurement sensitivity on $g_s g_p$. On the other hand, the lower end of this range is constrained by the wavelength of UCNs and the surface property of the electrodes, such as the surface roughness, which was in the range of a few hundred nm, or the diamond-like-carbon coating that has a thickness of a few μm and a nucleon density between those of the aluminum and the copper electrodes.

Figure 6 shows the upper limits of $g_s g_p$ constrained by the most recent measurements covering an interaction range of $1 \mu\text{m} < \lambda < 1$ mm. The upper horizontal axis displays the corresponding mass of an ALP m_{ALP} , with $\lambda = \hbar / (m_{\text{ALP}} c)$. The figure shows five measurement results, labeled from A to E. A is the limit obtained from this work (equation (29)), whereas E is obtained from our previous experiment [48]. Both experiments were based on a clock comparison of precession frequencies between polarized UCNs and ^{199}Hg atoms. An improvement in the sensitivity by a factor of 2.7 was accomplished, which is the current best limit of $g_s g_p$ obtained with UCNs. Additionally, we estimated the sensitivity of a new experiment, n2EDM, which is currently under construction at the PSI, to the SRSD interaction. The projected sensitivity is shown as B, and details of improvements on different statistical and systematic aspects are given in section 5. C is the result based on the comparison of spin-precession-frequency shifts of cohabiting ^3He and ^{129}Xe atoms, in the presence of an unpolarized mass of BGO ($\text{Bi}_4\text{Ge}_3\text{O}_{12}$) crystal [75]. D results from the comparison of nuclear-magnetic-resonance-frequency shifts of cohabiting polarized ^{129}Xe and ^{131}Xe atoms in the presence of a nonmagnetic zirconium rod [76]. F is the result from the measurement of anomalous spin relaxation of polarized ^3He atoms induced by an additional depolarization channel, which might be caused by the pseudomagnetic field generated from the ^3He -cell walls [50].

5. Prospects for ALP measurements in the n2EDM experiment

A new experiment, n2EDM, to search for a permanent nEDM is currently under construction at the PSI. The aim is to search for an nEDM with a sensitivity of about $1 \times 10^{-27} e \cdot \text{cm}$ [77, 78]. This will be accomplished by improved statistical sensitivity and an improved control of systematic effects. The apparatus can also be used to search for an SRS interaction mediated by ALPs.

The n2EDM apparatus features two precession chambers mounted on top of each other. This stack is made of three electrodes from aluminum spaced vertically by a height of 12 cm. In between the electrodes, cylindrical rings made of isolating polystyrene with a diameter of 80 cm [78] define the two precession chambers, increasing the volume of each precession chamber by a factor of three (a factor of six in total). The double-chamber design allows a simultaneous measurement in both chambers with opposite electric-field polarities while being exposed to the same magnetic-field direction. Without applying an electric field, it may be used for a refined search for a SRS interaction with improved statistical and systematic sensitivities. In the following paragraphs, we estimate possible improvements in statistical and systematic sensitivity with respect to the above presented measurement.

The statistical sensitivity of $\mathcal{R} = f_n/f_{\text{Hg}}$ has contributions from neutron counting statistics and the uncertainty of the mercury-precession signal. With an optimized connection from the UCN source to the experiment and the double chamber with a factor of six larger total volume for UCNs, the projected number of detected neutrons after a free precession time of $\mathcal{T} = 180$ s will increase by a factor of eight. At the same time, the fringe visibility α slightly improves to 0.8 [78]. Together, this will result in an improvement on the sensitivity of f_n by a factor of three, corresponding to a magnetic-field sensitivity of 110 fT. The sensitivity of the mercury magnetometer is expected to be at least $\sigma_{B_{\text{Hg}}} = 30$ fT per cycle [78]. Hence, we expect a factor of six in statistical improvement to 0.2 ppm. Recall that unexplained noise decreased the expected statistical sensitivity by a factor of 4–5 in the search presented in this article.

The largest uncertainty in the current result stems from the vertical magnetic-field gradient G_{grav} . Assuming that G_{grav} will be expanded up to fifth degree (equation (10)), we expect the uncertainties of $G_{1,0}$, $G_{3,0}$, and $G_{5,0}$ determined by the HgM, the CsM array, and a more reproducible magnetic-field maps, respectively, to be [78]

$$\begin{aligned}\sigma_{G_{1,0}} &\leq \sqrt{2} \sigma_{B_{\text{Hg}}}/H' \approx 2.4 \text{ fT cm}^{-1}, \\ \sigma_{G_{3,0}} &\leq 36 \times 10^{-3} \text{ fT cm}^{-3}, \quad \text{and} \\ \sigma_{G_{5,0}} &\leq 20 \times 10^{-6} \text{ fT cm}^{-5},\end{aligned}\tag{30}$$

where $H' = 18$ cm is the distance between the centers of the upper and the lower precession chambers. Summing up all contributions, this implies a systematic uncertainty of $\sigma_{G_{\text{grav}}} \approx 50 \text{ fT cm}^{-1}$ on the vertical magnetic-field gradient; an improvement by a factor of 80 from the average uncertainty of about 4 pT cm^{-1} presented in this article.

The transverse magnetic field was estimated with field maps [63]. In n2EDM, field maps will be used to measure all higher gradients above $G_{3,0}$, with a reproducibility requirement matching the previous repeatability [78]. This results in a tenfold improvement of the uncertainty $\sigma_{\langle B_i^2 \rangle}$.

By using a linearly polarized light scheme for reading out the mercury precession, we can suppress entirely the direct light shift. The vector light shift can be partially suppressed and characterized in dedicated measurements and will not significantly contribute to an overall error budget [79].

In summary, assuming perfect scaling of various aspects described above to hold without introducing new uncertainties, this results in a measurement of \mathcal{R} with a statistical precision of about $\sigma_{\text{stat}}^{\text{n2EDM}} = 2 \times 10^{-7}$ and a systematic precision of about $\sigma_{\text{sys}}^{\text{n2EDM}} = 4 \times 10^{-8}$, more than one order of magnitude improvement compared to (25) [62]. With the estimated improvements on the statistical and, in particular, on the gradient-induced systematic uncertainties, we anticipate a factor of three improvement to $g_s g_p \lambda^2 < 3 \times 10^{-28} \text{ m}^2$ when using three electrodes all made of aluminum. This might seem astonishing, considering the 25 times sensitivity gain on the measurement of the pseudomagnetic field estimated with equation (27). However, in the new experiment, the center-of-mass offsets individually estimated for each chamber are both $\langle z \rangle \approx 0.1$ cm, which are a factor of four smaller, reducing the sensitivity by a factor of three.

Note, that similar to the current experiment, using an asymmetric nucleon density between the upper and the lower boundary of each chamber, the sensitivity can be significantly increased. A possible approach might be placing thin copper sheets on the middle and the lower electrodes. With a 1 mm-thick copper sheet, the interaction range up to 1×10^{-3} m can be covered. In case of a null result, the prospected sensitivity would result in an upper limit on the product of the couplings of better than $g_s g_p \lambda^2 < 1 \times 10^{-29} \text{ m}^2$ (95% C.L., marked as B in figure 6) when using copper having a 3.3 times larger nucleon density compared to aluminum.

6. Conclusion

This paper reports on the null result from a search for a hypothetical, SRSD interaction mediated by ALPs. UCNs were stored simultaneously with ^{199}Hg atoms in a cylindrical chamber sandwiched between a copper and an aluminum electrode in a constant vertical magnetic field in the same apparatus used to measure the neutron EDM at the PSI. By measuring the precession-frequency ratio $\mathcal{R} = f_n/f_{\text{Hg}}$ between UCNs and ^{199}Hg atoms in opposite magnetic-field directions, we searched for the SRSD interaction between nucleons of the electrodes and stored UCNs.

Systematic effects from magnetic-field gradients influenced the measurement of \mathcal{R} . The dominant effect arose from the center-of-mass offset between the two particle species in an effective vertical magnetic-field gradient G_{grav} . As \mathcal{R} is a linear function of G_{grav} , we intentionally applied a vertical magnetic-field gradient in the measurement and compared \mathcal{R} in different G_{grav} using the crossing-point analysis. For a better estimation on G_{grav} , we combined both the online CsM data and magnetic-field maps taken at a different time using a dedicated device for mapping. The optimal method to incorporate both results was determined using synthesized data. By applying this optimized method to measurement data, G_{grav} was estimated with an unprecedented precision of 4.05 pT cm^{-1} .

By extracting \mathcal{R} at $G_{\text{grav}} = 0$ after correcting for all known systematic effects, a new limit on the product of the scalar and the pseudoscalar couplings, corresponding to the monopole-dipole interaction, gives $g_s g_p \lambda^2 < 8.3 \times 10^{-28} \text{ m}^2$ (95% C.L.) in an interaction range of $5 \mu\text{m} < \lambda < 25 \text{ mm}$. This limit improves our previous experiment by a factor of 2.7, the best limit obtained with free neutrons.

With the n2EDM apparatus at the PSI, we plan to search for a nonzero nEDM with a sensitivity of about $1 \times 10^{-27} e \cdot \text{cm}$. By comparing the precession frequencies of ^{199}Hg atoms and the UCNs in the new spectrometer, a new, more than one order of magnitude more accurate measurement of the gyromagnetic ratios $\gamma_n/\gamma_{\text{Hg}}$ becomes possible. Further, a refined search of ALPs by placing a 1 mm-thick copper layer on the corresponding bottom electrode of each chamber seems attractive. A new upper limit of $g_s g_p \lambda^2 < 1 \times 10^{-29} \text{ m}^2$ (95% C.L.), a factor of 80 better than the result presented here, could be expected.

Data availability statement

The data cannot be made publicly available upon publication because they are not available in a format that is sufficiently accessible or reusable by other researchers. The data that support the findings of this study are available upon reasonable request from the authors.

Acknowledgments

We acknowledge the excellent support provided by the PSI technical groups and by various services of the collaborating universities and research laboratories. In particular, we acknowledge with gratitude the long term outstanding technical support by F Burri and M Meier. We thank the UCN source operation group BSQ for their support. We acknowledge financial support from the Swiss National Science Foundation through Project Nos. 117696, 137664, 144473, 157079, 172626, 126562, 169596, 178951 (all PSI), 181996 (Bern), 162574 and 172639 (both ETH). The group from Jagiellonian University Cracow acknowledges the support from the National Science Center, Poland, through Grant Nos. UMO-2015/18/M/ST2/00056, UMO-2020/37/B/ST2/02349 and 2018/30/M/ST2/00319, as well as by the Excellence Initiative—Research University Program at the Jagiellonian University. This work was supported by the Research Foundation-Flanders (BE) under Grant No. G.0D04.21 N. We acknowledge the support from the DFG (DE) on PTB core facility center of ultra-low magnetic field KO 5321/3-1 and TR 408/11-1. We acknowledge funding provided by the Institute of Physics Belgrade through a grant by the Ministry of Education, Science and Technological Development of the Republic of Serbia. This work is also supported by Sigma Xi Grants # G2017100190747806 and # G2019100190747806, and by the award of the Swiss Government Excellence Scholarships (SERI-FCS) # 2015.0594.

ORCID iDs

K Bodek  <https://orcid.org/0000-0002-2866-2837>

P-J Chiu  <https://orcid.org/0000-0002-3772-0090>

M Fertl  <https://orcid.org/0000-0002-1925-2553>

P Mohanmurthy  <https://orcid.org/0000-0002-7573-7010>

P Schmidt-Wellenburg  <https://orcid.org/0000-0001-5474-672X>

References

- [1] Tanabashi M et al 2018 *Phys. Rev. D* **98** 030001
- [2] Zyla P A et al 2020 *Prog. Theor. Exp. Phys.* **2020** 083C01
- [3] Bartelmann M 2010 *Rev. Mod. Phys.* **82** 331
- [4] Sakharov A D 1991 *Sov. Phys. - Usp.* **34** 392
- [5] Kobayashi M and Maskawa T 1973 *Prog. Theor. Phys.* **49** 652
- [6] Maki Z, Nakagawa M and Sakata S 1962 *Prog. Theor. Phys.* **28** 870
- [7] Christenson J H, Cronin J W, Fitch V L and Turlay R 1964 *Phys. Rev. Lett.* **13** 138
- [8] Fanti V et al 1999 *Phys. Lett. B* **465** 335
- [9] Alavi-Harati A et al 1999 *Phys. Rev. Lett.* **83** 22
- [10] Wahl H 2004 *Phys. Rep.* **403–404** 19
- [11] Aubert B et al 2001 *Phys. Rev. Lett.* **86** 2515
- [12] Abe K et al 2001 *Phys. Rev. Lett.* **87** 091802
- [13] Höcker A, Lacker H, Laplace S and Le Diberder F 2002 *AIP Conf. Proc.* **618** 27
- [14] Morrissey D E and Ramsey-Musolf M J 2012 *New J. Phys.* **14** 125003
- [15] 't Hooft G 1976 *Phys. Rev. Lett.* **37** 8
- [16] 't Hooft G 1976 *Phys. Rev. D* **14** 3432
- [17] Weinberg S 1978 *Phys. Rev. Lett.* **40** 223
- [18] Peccei R D and Quinn H R 1977 *Phys. Rev. Lett.* **38** 1440
- [19] Wilczek F 1978 *Phys. Rev. Lett.* **40** 279
- [20] Moody J E and Wilczek F 1984 *Phys. Rev. D* **30** 130
- [21] Kim J E 1979 *Phys. Rev. Lett.* **43** 103
- [22] Kim J E and Carosi G 2010 *Rev. Mod. Phys.* **82** 557
- [23] Fayet P 1990 *Nucl. Phys. B* **347** 743
- [24] Fayet P 1996 *Class. Quantum Grav.* **13** A19
- [25] Jaeckel J and Ringwald A 2010 *Annu. Rev. Nucl. Part. Sci.* **60** 405
- [26] Svrcek P and Witten E 2006 *J. High Energy Phys.* **2006** 051
- [27] Arias P, Cadamuro D, Goodsell M, Jaeckel J, Redondo J and Ringwald A 2012 *J. Cosmol. Astropart. Phys.* **JCAP06(2012)013**
- [28] Sikivie P 2021 *Rev. Mod. Phys.* **93** 015004
- [29] Brun P 2013 *J. Phys.: Conf. Ser.* **460** 012015
- [30] Bartram C et al 2021 *Phys. Rev. Lett.* **127** 261803
- [31] Jewell M J et al 2023 *Phys. Rev. D* **107** 072007
- [32] CAST Collaboration 2017 *Nat. Phys.* **13** 584
- [33] Aybas D et al 2021 *Phys. Rev. Lett.* **126** 141802
- [34] Roussy T S et al 2021 *Phys. Rev. Lett.* **126** 171301
- [35] Ouellet J L et al 2019 *Phys. Rev. Lett.* **122** 121802
- [36] Ehret K et al 2010 *Phys. Lett. B* **689** 149
- [37] Ballou R et al 2015 *Phys. Rev. D* **92** 092002
- [38] Rong X et al 2018 *Nat. Commun.* **9** 739
- [39] Wang Y et al 2022 *Phys. Rev. Lett.* **129** 051801
- [40] Zimmer O 2010 *Phys. Lett. B* **685** 38
- [41] Serebrov A P et al 2010 *JETP Lett.* **91** 6
- [42] Abel C et al 2020 *Phys. Rev. Lett.* **124** 081803
- [43] Abel C et al 2017 *Phys. Rev. X* **7** 041034
- [44] nEDM Collaboration at PSI 2021 *Phys. Lett. B* **812** 135993
- [45] Bison G et al 2020 *Eur. Phys. J. A* **56** 33
- [46] Lauss B and Blau B 2021 *SciPost Phys. Proc.* **5** 004
- [47] Afach S et al 2015 *Phys. Rev. Lett.* **115** 162502
- [48] Afach S et al 2015 *Phys. Lett. B* **745** 58
- [49] Chiu P-J 2021 Search for a new interaction mediated by axionlike particles *PhD Thesis* ETH Zurich
- [50] Guigüe M, Jullien D, Petukhov A K and Pignol G 2015 *Phys. Rev. D* **92** 114001
- [51] Lide D R 2004 *CRC Handbook of Chemistry and Physics* (CRC Press)
- [52] Green K et al 1998 *Nucl. Instrum. Methods Phys. Res. A* **404** 381
- [53] Ban G et al 2018 *Nucl. Instrum. Methods Phys. Res. A* **896** 129
- [54] Bodek K et al 2008 *Nucl. Instrum. Methods Phys. Res. A* **597** 222
- [55] Atchison F et al 2006 *Phys. Rev. C* **74** 055501
- [56] Atchison F et al 2007 *Phys. Rev. C* **76** 044001
- [57] Abel C et al 2020 *Phys. Rev. A* **101** 053419
- [58] Afach S et al 2014 *J. Appl. Phys.* **116** 084510
- [59] Ramsey N F 1950 *Phys. Rev.* **78** 695
- [60] Afach S et al 2015 *Eur. Phys. J. A* **51** 143
- [61] Ban G et al 2016 *Eur. Phys. J. A* **52** 326
- [62] Afach S et al 2014 *Phys. Lett. B* **739** 128
- [63] Abel C et al 2022 *Phys. Rev. A* **106** 032808
- [64] Bloch F and Siegert A 1940 *Phys. Rev.* **57** 522
- [65] Ramsey N F 1955 *Phys. Rev.* **100** 1191
- [66] Abel C et al 2019 *Phys. Rev. A* **99** 042112
- [67] Johnson J B 1928 *Phys. Rev.* **32** 97
- [68] Nyquist H 1928 *Phys. Rev.* **32** 110
- [69] Harris P G, Pendlebury J M and Devenish N E 2014 *Phys. Rev. D* **89** 016011
- [70] Afach S et al 2015 *Phys. Rev. D* **92** 052008
- [71] Fertl M 2013 A laser based mercury co-magnetometer for the neutron electric dipole moment search *PhD Thesis* ETH Zürich

- [72] Sears V F 1992 *Neutron News* **3** 26
- [73] Chanel E G A 2021 The BeamEDM experiment and the measurement of the neutron incoherent scattering length of ^{199}Hg *PhD Thesis* Philosophisch-naturwissenschaftliche Fakultät der Universität Bern
- [74] Ayres N J *et al* 2021 *Phys. Rev. A* **103** 062801
- [75] Tullney K *et al* 2013 *Phys. Rev. Lett.* **111** 100801
- [76] Bulatowicz M *et al* 2013 *Phys. Rev. Lett.* **111** 102001
- [77] Abel C *et al* 2019 *EPJ Web Conf.* **219** 02002
- [78] Ayres N J *et al* 2021 *Eur. Phys. J. C* **81** 512
- [79] Cohen-Tannoudji C 1962 *Ann. Phys.* **13** 423